Mon. Not. R. Astron. Soc. **385,** 519–530 (2008) doi:10.1111/j.1365-2966.2008.12860.x

Tracing the gas at redshift 1.7–3.5 with the Lyα forest: the FLO approach*

F. Saitta,[1,2,3]† V. D'Odorico,[1] M. Bruscoli,[1,4] S. Cristiani,[1,5] P. Monaco[1,3] and M. Viel[1,5]

[1]*INAF – Osservatorio Astronomico di Trieste, via Tiepolo 11, I-34143 Trieste, Italy*
[2]*European Southern Observatory, Karl-Schwarzschil-Str. 2, D-85748 Garching, Germany*
[3]*Dipartimento di Astronomia, Università di Trieste, via Tiepolo 11, I-34143 Trieste, Italy*
[4]*INAF-IRA, Largo E. Fermi 5, I-50125 Firenze, Italy*
[5]*INFN/National Institute for Nuclear Physics, Via Valerio 2, I-34127 Trieste, Italy*

Accepted 2007 December 14. Received 2007 December 14; in original form 2007 June 6

ABSTRACT

We present FLO (From Lines to Overdensities), a new technique to reconstruct the hydrogen density field for the Lyα forest lines observed in high-resolution QSO spectra. The method is based on the hypothesis that the Lyα lines arise in the low to intermediate density intergalactic gas and that the Jeans length is the typical size of the Lyα absorbers. The reliability of FLO is tested against mock spectra obtained from cosmological simulations. The recovering algorithm gives satisfactory results in the range from the mean density to overdensities of $\sim$30 and reproduces correctly the correlation function of the density field and the 1D power spectrum on scales between $\sim$20 and 60 comoving Mpc. A sample of Lyα forests from 22 high-resolution QSO spectra is analysed, covering the redshift range $1.7 \lesssim z \lesssim 3.5$. For each line of sight, we fit Voigt profiles to the lines of the Lyα forest, providing the largest, homogeneous sample of fitted Lyα lines ever studied. The line number density evolution with redshift follows a power-law relation: $\mathrm{d}n/\mathrm{d}z = (166 \pm 4)\,[(1+z)/3.5]^{(2.8\pm0.2)}$ (1σ errors). The two-point correlation function of lines shows a signal up to separations of $\sim$2 comoving Mpc; weak lines [$\log N(\mathrm{H\,i}) < 13.8$] also show a significant clustering but on smaller scales ($r \lesssim 1.5$ comoving Mpc). We estimate with FLO the hydrogen density field toward the 22 observed lines of sight. The redshift distribution of the average densities computed for each QSO is consistent with the cosmic mean hydrogen density in the analysed redshift range. The two-point correlation function and the 1D power spectrum of the δ field are estimated. They are both consistent with the analogous results computed from hydrosimulated spectra obtained in the framework of the concordance cosmological model. The correlation function shows clustering signal up to $\sim$4 comoving Mpc.

Key words: intergalactic medium – quasars: absorption lines – cosmology: observations – large-scale structure of Universe.

1 INTRODUCTION

Semi-analytical and hydrodynamical simulations (e.g. Cen et al. 1994; Zhang, Anninos & Norman 1995; Hernquist et al. 1996; Miralda-Escudé et al. 1996; Bi & Davidsen 1997; Davé et al. 1997; Zhang et al. 1997; Theuns, Leonard & Efstathiou 1998; Machacek et al. 2000) suggest that the Lyα forest arises from fluctuations of the low-density intergalactic medium (IGM) that trace the underlying matter density field over cosmic time. The dynamical state of the low-density IGM is governed mainly by the Hubble expansion and by gravitational instabilities. As a consequence, the physics involved is quite simple and mildly non-linear. The statistical analysis of the Lyα forest provides information on the dynamical growth and thermal state of the IGM, and on the correlation properties of the (dark) matter in the Universe. Correlations of the Lyα forest lines were detected with a 4–5σ confidence by various authors at typical scales $\Delta v \lesssim 350$ km s^{-1} observing at high-resolution individual lines of sight (Cristiani et al. 1995; Lu et al. 1996 at $z \sim 3.7$;

*Based on observations collected at the European Southern Observatory Very Large Telescope, Cerro Paranal, Chile – Programmes 166.A-0106(A) and during commissioning and science verification of UVES.
†E-mail: fsaitta@eso.org

Cristiani et al. 1997 at $z \sim 3$; Kim, Cristiani & D'Odorico 2001 at $z \sim 2$). This velocity range corresponds to scales $\lesssim 2.5\,h^{-1}$ Mpc (assuming negligible peculiar velocities). The 'cosmic web' scenario (Bond, Kofman & Pogosyan 1996) is favoured against that of a population of pressure confined clouds (Sargent et al. 1980) thanks also to the analysis of the line correlation observed in close pairs of QSO lines of sight, implying absorber sizes of a few hundred kpc (e.g. Smette et al. 1992; Bechtold et al. 1994; Smette et al. 1995; Fang et al. 1996; Dinshaw et al. 1997; Crotts & Fang 1998; Petitjean et al. 1998; D'Odorico et al. 1998; Rauch et al. 2001; Young, Impey & Foltz 2001; Becker, Sargent & Rauch 2004). The analysis of multiple lines of sight at slightly larger separations (smaller than a few arcminutes), makes it possible to compute the transverse correlation function for which a clustering signal is detected up to velocity separations of $\sim$200 km s^{-1}, or about $3h^{-1}$ comoving Mpc (e.g. Rollinde et al. 2003; Coppolani et al. 2006; D'Odorico et al. 2006).

Traditionally, absorption spectra were decomposed into Voigt profiles which were then identified with individual discrete absorption systems. Information on the physical state of the gas originating the absorptions comes directly from the fit parameters: redshift, column density and Doppler broadening (linked to the temperature). In the new paradigm the emphasis of the analysis has shifted to statistical measures of the transmitted flux (e.g. the flux power spectrum) more suitable for absorption arising from a continuous density field. However, the interpretation of statistical quantities of the continuous flux field and their relation with the physical properties of the gas requires a non-trivial comparison with full hydrodynamical high-resolution simulations that are computationally expensive.

The aim of this paper is to extend the line-fitting approach by identifying a new statistical estimator linked to the physical properties of the underlying IGM. This new estimator will also overcome the two main drawbacks of the Voigt fitting method:

(i) the subjectivity of the decomposition into components: the same absorption can be resolved by different scientists (or software tools) in different ways, both in the number of components, and in the values of the output parameters for a single component;

(ii) the blanketing effect of weak lines: they can be hidden by the stronger lines, so that their exact number density is unknown and has to be inferred from statistical arguments. Unfortunately, since the weak lines are also the most numerous, the uncertainty in their exact number is transformed into a systematic error of the computed statistical quantities.

This new estimator is identified in the hydrogen density field, $n_{\rm H}$, which is linked to the measured H I column densities through the formula (Schaye 2001)

$$N(\mathrm{H\,I}) \simeq 3.7 \times 10^{13}\,\mathrm{cm}^{-2}(1+\delta)^{1.5-0.26\alpha} T_{0,4}^{-0.26}\Gamma_{12}^{-1} \times \left(\frac{1+z}{4}\right)^{9/2}\left(\frac{\Omega_{\rm b}h^2}{0.024}\right)^{3/2}\left(\frac{f_{\rm g}}{0.178}\right)^{1/2}, \quad (1)$$

where $\delta \equiv n_{\rm H}/\langle n_{\rm H}\rangle - 1$ is the density contrast, $T_{0,4} \equiv T_0/10^4$ is the temperature at the mean density, $\Gamma_{12} \equiv \Gamma/10^{-12}$ is the H photoionization rate, $f_{\rm g} \approx \Omega_{\rm b}/\Omega_{\rm m}$ is the fraction of the mass in gas and α depends on the ionization history of the Universe. Equation (1) relies on three main hypotheses: (i) Lyα absorbers are close to local hydrostatic equilibrium, i.e. their characteristic size will be typically of the order of the local Jeans length ($L_{\rm J}$); (ii) the gas is in photoionization equilibrium; (iii) the equation of state, $T = T_0(\delta+1)^{\alpha}$ holds for the optically thin IGM gas (Hui & Gnedin 1997).

The procedure to recover the H density field from the list of Lyα line column densities in a QSO line of sight, has been dubbed FLO (From Lines to Overdensities).

The paper is organized as follows. Section 2 describes the observed data sample used for our analysis and presents the statistical measures obtained for the fitted Lyα lines; Section 3 introduces the hydrogen density field as a statistical estimator, and describes the construction algorithm; Section 4 presents the simulated spectra and the test of reliability of the method with this data set; in Section 5 the new algorithm is applied to the observed data sample; finally, we draw our conclusions in Section 6.

The cosmological model adopted throughout this paper corresponds to a 'fiducial' ΛCDM universe with parameters, at $z = 0$, $\Omega_{\rm m} = 0.26$, $\Omega_{\Lambda} = 0.74$, $\Omega_{\rm b} = 0.0463$, $n_{\rm s} = 0.95$, $\sigma_8 = 0.85$ and $H_0 = 72$ km s^{-1} Mpc^{-1} (the B2 set of parameters of Viel, Haehnelt & Springel 2004).

2 OBSERVED DATA SAMPLE

Most of the observational data used in this work were obtained with the UVES spectrograph (Dekker et al. 2000) at the Kueyen unit of the ESO VLT (Cerro Paranal, Chile) in the framework of the ESO Large Programme (LP): 'The Cosmic Evolution of the IGM' (Bergeron et al. 2004). Spectra of 18 QSOs were obtained in service mode with the aim of studying the physics of the IGM in the redshift range 1.7–3.5. The spectra have a resolution $R \sim 45\,000$ and a typical signal-to-noise ratio (S/N) of $\sim$35 and 70 per pixel at 3500 and 6000 Å, respectively. Details of the data reduction can be found in Aracil et al. (2004) and Chand et al. (2004).

We added to the main sample four more QSO spectra with comparable resolution and S/N.

(i) J2233−606 (Cristiani & D'Odorico 2000): Data for this QSO were acquired during the commissioning of UVES in 1999 October.

(ii) HE1122−1648 (Kim et al. 2002): Data for this QSO were acquired during the science verification of UVES in 2000 February. The reduced and fitted spectrum was kindly provided to us by Tae-Sun Kim.

(iii) HS1946+7658 (Kirkman & Tytler 1997): Data for this QSO were acquired with Keck/HIRES in 1994 July.

(iv) B1422+231 (Rauch et al. 1996): Data for this QSO were acquired with Keck/HIRES in 1996. The reduced and fitted spectrum was kindly provided to us by Tae-Sun Kim.

Table 1 summarizes the main properties of our QSO sample. None of our QSOs is a broad absorption-line object. Magnitudes are taken from the GSC-II catalogue (McLean et al. 2000). Fig. 1 shows the distribution in redshift of the Lyα forests for all the QSOs of the sample. We considered for each QSO the redshift range between 1000 km s^{-1} redward of the Lyβ emission, in order to avoid contamination by associated Lyβ lines, and 5000 km s^{-1} blueward of the Lyα emission to exclude the region affected by the proximity effect due to the ionizing flux of the QSO. The coverage is good over the whole redshift range $z \simeq 1.7$–3.5, with most of the signal concentrated between $z \sim 2$ and 2.5. In Fig. 2, we show a portion of the Lyα forest of the QSO HE0001−2340 compared with the same wavelength region in a mock spectrum extracted from the considered simulation box at $z = 2$ (see Section 4).

2.1 Creation of the line lists

All the lines in the Lyα regions of the LP QSOs plus J2233−606 were fitted with the FITLYMAN tool (Fontana & Ballester 1995) of

Table 1. Summary of the main characteristics of our QSO sample (see text).

QSO	z_{em}	J magnitude	Lyα Δz
HE1341−1020	2.139	18.68	1.658–2.087
Q0122−380	2.203	17.34	1.711–2.150
PKS1448−232	2.220	17.09	1.725–2.166
PKS0237−23	2.233	16.61	1.737–2.179
J2233−606	2.250	16.97	1.753–2.196
HE0001−2340	2.267	16.74	1.765–2.213
HE1122−1648	2.400	16.61	1.878–2.344
Q0109−3518	2.407	16.72	1.884–2.350
HE2217−2818	2.415	16.47	1.891–2.358
Q0329−385	2.440	17.20	1.912–2.383
HE1158−1843	2.451	17.09	1.921–2.394
HE1347−2457	2.560	17.35	2.016–2.502
Q0453−423	2.662	17.69	2.100–2.602
PKS0329−255	2.698	17.88	2.125–2.636
HE0151−4326	2.761	17.48	2.186–2.699
Q0002−422	2.768	17.50	2.189–2.705
HE2347−4342	2.878	17.12	2.281–2.814
HS1946+7658	3.051	16.64	2.429–2.984
HE0940−1050	3.088	17.08	2.463–3.020
Q0420−388	3.122	17.44	2.489–3.053
PKS2126−158	3.275	17.54	2.620–3.204
B1422+231	3.620	16.22	2.911–3.543

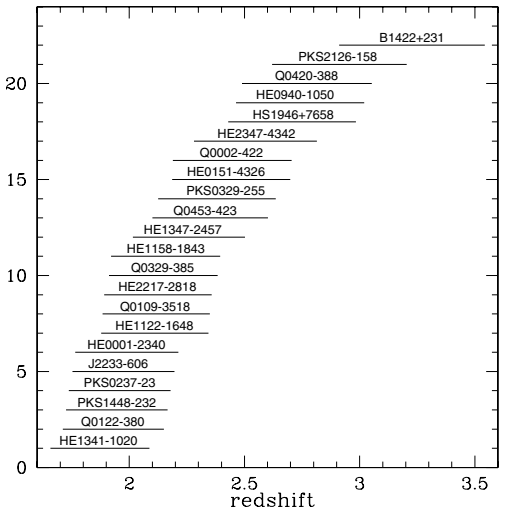

Figure 1. Lyα forest redshift coverage of the QSOs in our sample.

the ESO MIDAS data reduction package.[1] In the case of complex saturated lines we used the minimum number of components to reach $\chi^2 \leqslant 1.5$. Whenever possible, the other lines in the Lyman series were used to constrain the fit. The spectra of HE1122−1648, HS1946+7658, B1422+231 and all the simulated lines of sight were fitted with the VPFIT[2] package. Both software tools model absorption features with a Voigt profile convolved with the instrument line spread function. The minimum H I column density detectable at 3σ, at the lowest S/N of the spectra in our sample, is $\log N(\mathrm{H\,i}) \simeq 12\,\mathrm{cm}^{-2}$.

Metals in the forest were identified and the corresponding spectral regions were masked to avoid effects of line blanketing. We eliminated Lyα lines with Doppler parameters $b \leqslant 10$ km s^{-1}, that

[1] http://www.eso.org/midas.

[2] http://www.ast.cam.ac.uk/∼rfc/vpfit.html.

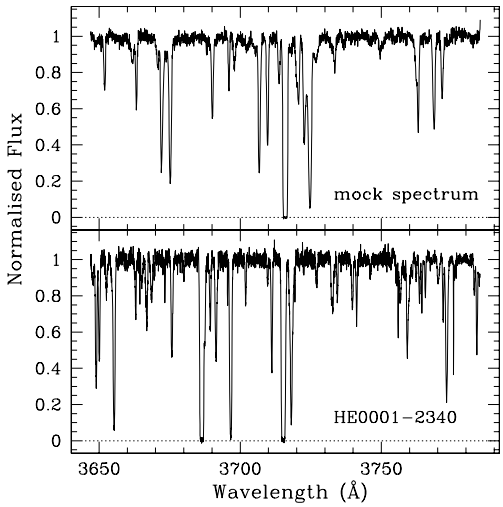

Figure 2. Portion of the Lyα forest for an observed (lower panel) and a simulated (upper panel) line of sight in our sample.

are likely unidentified metal absorptions. In a total amount of 8435 fitted Lyα lines, 368 (4.4 per cent) fall in the masked intervals, 1150 (13.6 per cent) are at less than 1000 km s^{-1} redward the Lyβ emission or at less than 5000 km s^{-1} blueward the Lyα emission, while 599 were eliminated because they have $b \leqslant 10$ (7.1 per cent). The output of this analysis is a list of Lyα lines for each QSO with central redshift, H I column density and Doppler parameter.

In the line-fitting approach to the study of the Lyα forest, each line is considered as the signature of an absorber. As a consequence statistical measures are computed with the population of absorption lines, representative of the population of absorbers. Our sample of fitted Lyα lines is the largest, homogeneous sample ever gathered up to now. We will use it to compute the number density evolution with redshift and the two-point correlation function (TPCF) of lines.

2.2 Line number density evolution

The line number density per unit of redshift is generally approximated as $\mathrm{d}n/\mathrm{d}z = (\mathrm{d}n/\mathrm{d}z)_0(1+z)^\beta$, where $(\mathrm{d}n/\mathrm{d}z)_0$ is the local comoving line number density of the forest and the exponent β depends both on physical (redshift, column density interval) and instrumental (spectral resolution, decomposition of velocity profiles) factors.

In Fig. 3 we plot the result for the QSOs in our sample for the standard column density interval $13.64 < \log N(\mathrm{H\,i}) < 17\,\mathrm{cm}^{-2}$ in order to compare our statistics with the *HST* low-redshift measurement[3] (Weymann et al. 1998). The best fit to our data gives $\mathrm{d}n/\mathrm{d}z = (166 \pm 4)\,[(1+z)/3.5]^{2.8\pm0.2}$ (1σ errors). There is no substantial change in the trend with respect to previous results by Kim and collaborators (2001, 2002) who used smaller samples of UVES QSO spectra of the same quality. However, our points are systematically higher on the plot, with an increase in $\log \mathrm{d}n/\mathrm{d}z$ amounting to ∼0.03 at $z \sim 2$ up to ∼0.1 at $z \sim 3$. The discrepancy arises from the fact that we have taken into account the decrease in the available

[3] The lower limit in column density is due to the fact that *HST* measurements have been transformed from equivalent width into H I column densities assuming a typical Doppler parameter of 30 km s^{-1}.

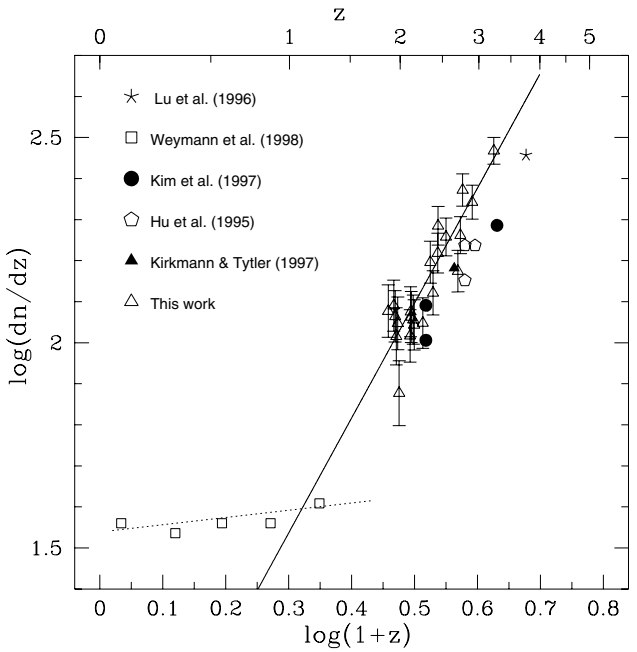

Figure 3. Number density evolution of the Lyα forest lines over the column density range $13.64 < \log N(\mathrm{H\,I}) < 17\,\mathrm{cm}^{-2}$ for the 22 QSOs in our sample (open triangles). The solid line traces the best linear fit obtained for those data (see text). For comparison, we report also previous measurements at high redshift and the result of the low-redshift *HST* campaign.

redshift interval due to the presence of metal lines 'masking' the Lyα features. High-resolution spectra allow us to identify a larger number of metal lines: in our sample these metal masks correspond to about 9 per cent of the total redshift interval covered by the observed Lyα forests.

Fig. 4 shows the number density evolution for two different H I column density ranges: $13 \leqslant \log N(\mathrm{H\,I}) \leqslant 14$ and $14.5 \leqslant \log N(\mathrm{H\,I}) < 17\,\mathrm{cm}^{-2}$. The linear fit in these intervals gives slopes of 1.9 ± 0.2 and 3.8 ± 0.4 for the weak and the strong lines selection, respectively. This trend was already noticed by Kim et al. (2002): stronger lines have a steeper number density evolution than the weaker ones.

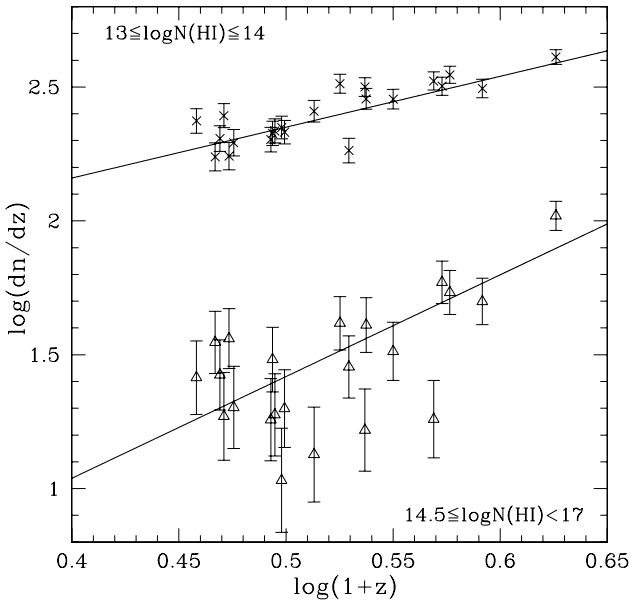

Figure 4. Number density evolution of the Lyα forest lines over the two column density ranges $13 \leqslant \log N(\mathrm{H\,I}) \leqslant 14$ (crosses) and $14.5 \leqslant \log N(\mathrm{H\,I}) < 17\,\mathrm{cm}^{-2}$ (open triangles) for the 22 QSOs in our sample. The lines are the best linear fits for the two distributions (see text).

2.3 Two-point correlation function of Lyα lines

To study the clustering properties of our sample of Lyα lines, we adopt the standard TPCF defined as the excess, due to clustering, of the probability dP of finding a Lyα absorber in a volume dV at a distance r from another absorber: $\mathrm{d}P = \Phi_{\mathrm{Ly}\alpha}(z)\,\mathrm{d}V\,[1 + \xi(r)]$, where $\Phi(z)$ is the average space density of the absorbers as a function of z.

Operatively this quantity is estimated with the formula (Peebles 1980)

$$\xi(v) = \frac{N_{\mathrm{obs}}(v)}{N_{\mathrm{exp}}(v)} - 1, \tag{2}$$

where N_{obs} is the observed number of line pairs with velocity separations between v and $v + \mathrm{d}v$, and N_{exp} is the number of pairs expected in the same range of separations from a random distribution in redshift. Since in this context peculiar velocities are negligible (see e.g. Rauch et al. 2005), we compute the correlation function in real space, measuring separations in comoving Mpc. At the characteristic redshift of our sample, $z = 2.5$, a velocity separation $\Delta v = 100\,\mathrm{km\,s}^{-1}$ corresponds to $\Delta r \simeq 0.9$ comoving Mpc, in our fiducial cosmology. N_{exp} is obtained by averaging the results of 1000 numerical simulations of the number of lines observed in each QSO spectrum. In particular, the set of line redshifts is randomly generated in the same redshift interval as the data according to the observed distribution $\propto (1 + z)^{\beta}$, where we adopt the value $\beta = 2.8$ found in the previous section. The same mock line lists are used to estimate the error on the observed correlation function by determining the 1σ standard deviation of the correlation functions of the randomly distributed lines. Lines closer than 0.3 comoving Mpc are merged into a single line with redshift equal to the mean redshift, weighted with the column densities and column density equal to the sum of the column densities. The minimal separation is set by the intrinsic blending due to the typical width of the lines (see Giallongo et al. 1996).

We compute the correlation function for the whole data set (Fig. 5) and for two column density cuts (Fig. 6) to investigate the clustering properties of strong and weak lines. Previous results (Cristiani et al. 1995; Lu et al. 1996; Cristiani et al. 1997) already showed a significant clustering signal for strong absorptions, which is confirmed and strengthened by our data. Furthermore, we also see a significant clustering for the weak lines, consistent with previous results by Misawa et al. (2004). The amplitude is about one order of magnitude lower than for the stronger lines but the clustering signal in the first bin is significant at the 7σ level.

As already said in Section 1, the Jeans length (L_{J}) likely represents the typical size of IGM structures detected as Lyα absorptions. This length (varying from $\sim$1.2 to 1.6 comoving Mpc for the maximum and minimum redshift of our sample, respectively) is also comparable with the clustering scale of the Lyα lines as shown in Fig. 5 (upper panel) and Fig. 6. In order to verify that the clustering signal we are detecting is not only due to structures internal to the absorbers, we perform the following test. Lines with separation less than the local L_{J} are merged into a single line with column density equal to the sum of the column densities of the component features and redshift equal to the $N(\mathrm{H\,I})$-weighted mean of the component

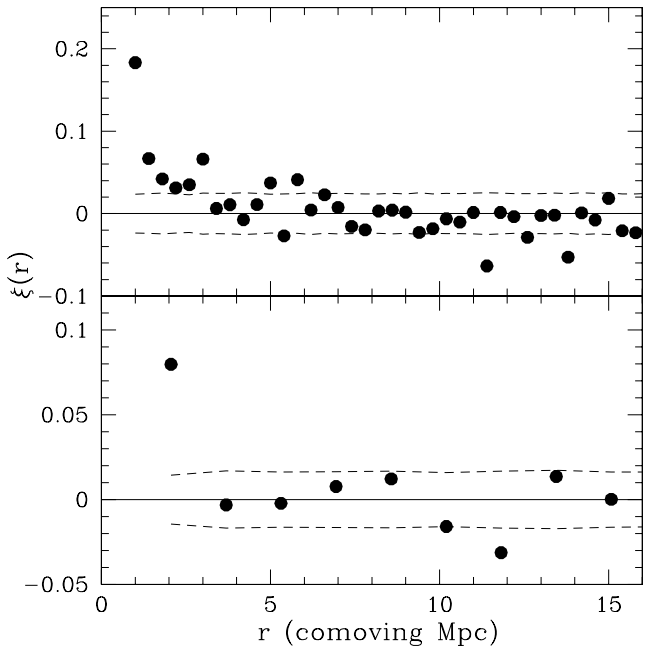

Figure 5. TPCF for the observed Lyα lines in the column density range $12 < \log N(\mathrm{H\,I}) < 17\ \mathrm{cm}^{-2}$. In the bottom panel lines closer than one Jeans length have been merged into one line, see text. The dashed lines represent the 1σ confidence levels from a random distribution of lines.

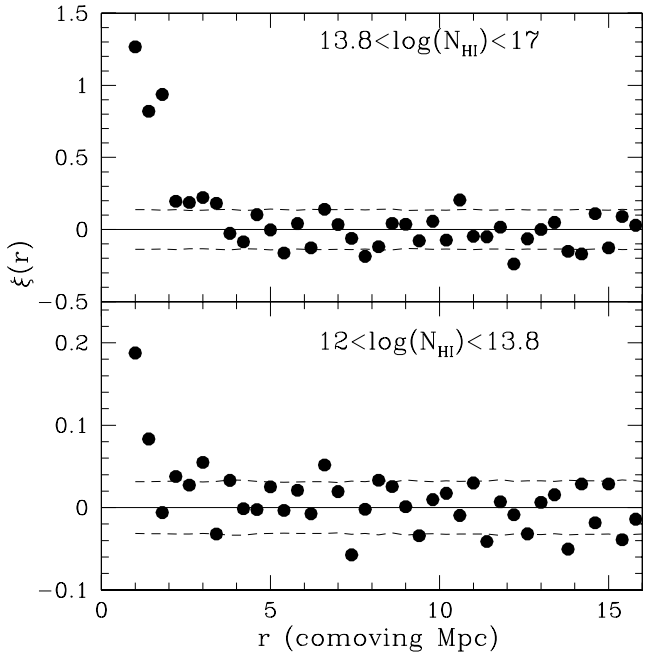

Figure 6. TPCF for the observed Lyα lines in two column density ranges as reported in the panels.

redshifts and the TPCF is recomputed. The result, reported in the lower panel of Fig. 5, shows that the clustering signal is preserved substantially at the same level of the one computed with all the lines, with a slightly decreased significance due to the smaller statistics. This is an indication that Lyα absorbers cluster among themselves and not only inside themselves.

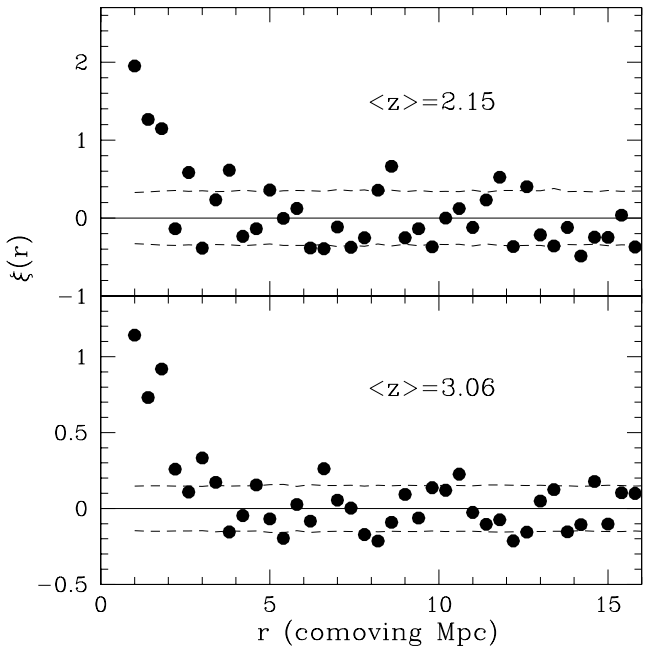

Figure 7. TPCF for the observed Lyα lines in the column density range $13.8 < \log N(\mathrm{H\,I}) < 17$ and in two redshift ranges reported in the panels.

The present data set is large enough to allow studying the evolution of the correlation function with redshift. We consider the column density range for which the signal is stronger, $13.8 < \log N(\mathrm{H\,I}) < 17$, and we divide our sample in two parts. The first subsample is formed by objects with emission redshift $z_{\rm em} \leqslant 2.5$, for which the average Lyα forest redshift is $\langle z_{\mathrm{Ly}\alpha} \rangle = 2.07$, and the second subsample has objects with $z_{\rm em} > 2.5$ and $\langle z_{\mathrm{Ly}\alpha} \rangle = 3.02$. Results are shown in Fig. 7: the high-redshift lines are less clustered than the low-redshift lines. This apparent evolution with redshift is biased by the fact that the relation $\delta - \log N(\mathrm{H\,I})$ is also z dependent. Indeed, the same column density range selects objects with a lower density contrast at higher redshift (see equation 1) explaining the lower clustering signal. To verify this effect, we selected lines on the ground of a constant density contrast, $\delta \gtrsim 3$, which corresponds to $\log N(\mathrm{H\,I}) > 13.8$ at the average redshift of the low-redshift subsample, and to $\log N(\mathrm{H\,I}) > 14.3$ at the higher average redshift. The correlation function for the latter subsample is shown in Fig. 8. Selecting the same kind of structures, there is no longer evidence of a significant evolution with redshift.

Table 2 shows a detailed budget of the number of lines used to compute the TPCF in all the different selections described above.

3 INTRODUCING FLO

In Section 1 we have described, on one hand, what are the main drawbacks of the two standard approaches (Voigt fitting and flux statistics) adopted to analyse the Lyα forest and derive statistical quantities describing the physical state of the IGM. On the other hand, the recovered H density field is introduced as a new robust estimator, whose statistical properties are in good agreement with those of the original density field, and which allows an easy comparison between observation and simulation results. The relation between the underlying H density field and the H I column densities

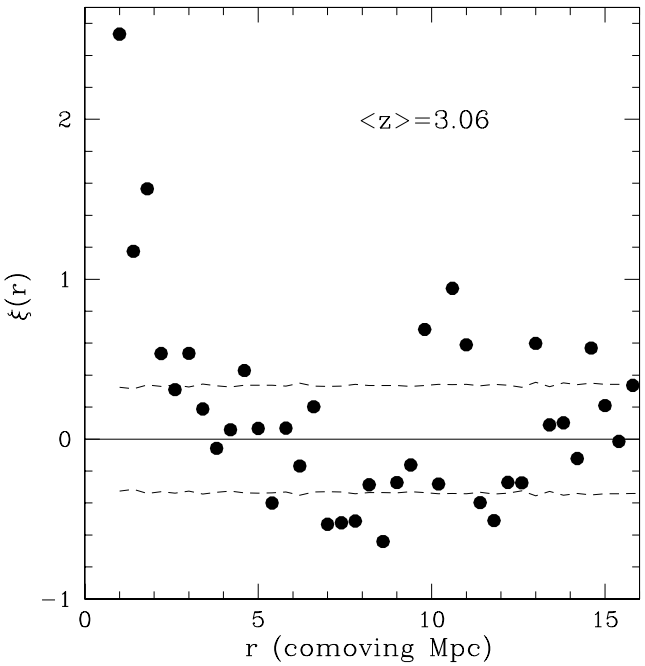

Figure 8. TPCF for the observed Lyα lines in the high-redshift range. Here the cut in column density is defined to correspond to a constant cut in density contrast, $\delta \gtrsim 3$, corresponding to $\log N(\mathrm{H\,I}) > 14.3$ at $z = 3.02$, see text.

measured for the observed absorption lines is summarized by equation (1).

Before describing the FLO technique in details, it is important to recall the main hypotheses.

(1) Lyα absorbers have typical sizes of the order of the local L_J, which can be approximated as (Zaroubi et al. 2006)

$$L_\mathrm{J} \simeq 1.33 \left(\frac{\Omega_\mathrm{m} h^2}{0.135}\right)^{-1/2} \left(\frac{T_0}{1.8 \times 10^4}\right)^{1/2} \times \left(\frac{1.6}{\alpha + 1}\right)^{1/2} \left(\frac{1+z}{4}\right)^{-1/2} \mathrm{Mpc} \quad (3)$$

in comoving units, where $h \equiv H_0/100\,\mathrm{km\,s^{-1}\,Mpc^{-1}}$, and the other parameters have been already defined.

(2) The IGM gas is in the linear or slightly non-linear regime [$\log(\delta + 1) \sim 1$, Hui & Gnedin 1997].

In order to apply equation (1) we have, first of all, to go through the Voigt fitting process of the Lyα forest absorptions in a QSO spectrum. Then, to transform the list of H I column densities of Lyα lines into the matter density field which generated them, we have to perform the following steps.

(1) Group Lyα lines into absorbers of size of 1 L_J with column density equal to the sum of column densities and redshift equal to the weighted average of redshifts, using column densities as weights. The absorbers are created with a friend-of-friend algorithm:

Table 2. Detailed budget of the number of lines used to compute TPCFs. The first column refers to the selection carried out, in terms of emission redshift of the considered objects.

Selection	N_QSO	Lyα lines							
		N^a_tot	N^b_mask	N^c_b	N^d_prox	N^e_comb	N^f_merg	N^g_col	N^h_fin
All QSOs $13.8 < \log N(\mathrm{H\,I}) < 17$ $\Delta r > 0.3$ comoving Mpc	22	8435	368	644	1150	1955	380	4953	1147
All QSOs $12 < \log N(\mathrm{H\,I}) < 13.8$ $\Delta r > 0.3$ comoving Mpc	22	8435	368	644	1150	1955	380	1319	4781
All QSOs $12 < \log N(\mathrm{H\,I}) < 17$ $\Delta r > 0.3$ comoving Mpc	22	8435	368	644	1150	1955	380	170	5930
$z_\mathrm{em} \leqslant 2.5$ $13.8 < \log N(\mathrm{H\,I}) < 17$ $\Delta r > 0.3$ comoving Mpc	11	3188	103	169	445	665	100	2042	381
$z_\mathrm{em} > 2.5$ $13.8 < \log N(\mathrm{H\,I}) < 17$ $\Delta r > 0.3$ comoving Mpc	11	5247	265	475	705	1290	280	2911	766
$z_\mathrm{em} > 2.5$ $14.3 < \log N(\mathrm{H\,I}) < 17$ $\Delta r > 0.3$ comoving Mpc	11	5247	265	475	705	1290	280	3345	332
All QSOs $12 < \log N(\mathrm{H\,I}) < 17$ $\Delta r > 1 L_\mathrm{J}$	22	8435	368	644	1150	1955	2944	64	3472

[a]Total number of fitted Lyα lines; [b]number of Lyα lines falling in the metal masks; [c]number of Lyα lines with $b < 10$ or $b > 100$; [d]number of lines falling closer than 1000 km s^{-1} redwards the Lyβ emission or closer than 5000 km s^{-1} bluewards the Lyα emission; [e]number of eliminated lines because one of the three previous conditions occurs; [f]number of merged lines because their separation is less than the Δr threshold indicated in the selection; [g]number of merged lines not fulfilling the column density selection; [h]number of lines used to compute the TPCF.

(i) the spatial separation between all the possible line pairs is computed and the minimum separation is compared with L_J, computed at the $N(\mathrm{H\,I})$-weighted redshift mean of the pair;

(ii) if the two lines of the pair are more distant than the local L_J, they are classified as two different absorbers, stored and deleted from the line list;

(iii) if the two lines are closer than the local L_J, they are replaced in the line list by one line with a redshift equal to the $N(\mathrm{H\,I})$-weighted mean of the two redshifts and a column density equal to the sum of the two column densities;

(iv) the procedure is iterated until all the lines are converted into absorbers.

(2) Transform the list of column densities of absorbers into a list of δ with equation 1.

(3) Bin the redshift range covered by the Lyα forest into steps of $1L_J$ and distribute the absorbers on to this grid, proportionally to the superposition between absorber size (which is again $1L_J$) and bin. Empty bins are filled with one absorber with hydrogen density contrast corresponding to the minimum detectable column density in our data, $\log N(\mathrm{H\,I}) = 12\ \mathrm{cm}^{-2}$ at the redshift of the bin.

(4) Normalize the resulting δ field in order to have $\langle \delta + 1 \rangle = 1.0$ for the whole considered sample. This operation is necessary to recover the correct asymptotic behaviour of the correlation function.

With the introduction of this new statistical estimator, the drawbacks of the standard Voigt fitting approach are significantly reduced. On one hand, the statistical weight of weak lines is reduced, since their contribution to the δ field is low. On the other hand, we verify that, in the process of Voigt fitting complex absorption features, the total H I column density is a much more robust quantity than the number of components. To this purpose, we compare the results of the line lists of a subsample of 12 QSOs adopted in the present work with the corresponding lists obtained with the VPFIT package, kindly provided to us by Tae-Sun Kim. The total number of lines in each line of sight is not conserved, in particular, significant differences are observed for the complex absorption systems where, in general, VPFIT fits more lines than FITLYMAN. Most of these discrepancies are due to the identification of low column density lines. However, the total column density in these complex absorbers appears to be much more stable between the two fitting methods.

In Fig. 9, we plot the comparison between FITLYMAN and VPFIT for one QSO of the sample, Q0109−3518 ($z_{\mathrm{em}} = 2.407$). We divide the line of sight into redshift bins of width $\Delta z = 0.01$; we sum both the number and the column densities of the lines in each bin, and plot them against redshift. It is evident that while the number of lines is different, the two column density distributions trace each other more faithfully.

VPFIT has been used to fit the lines of three QSOs in our sample (see Section 2) and also to analyse the output spectra from the simulation (see next section). We verify the stability of FLO against different fitting tools by applying it to the line lists obtained with VPFIT and with FITLYMAN for the 12 common QSOs. In Fig 10, we show the comparison between the two recovered fields by means of a contour scatter plot. The correlation is tight for all values of δ, the scatter increases slightly for $\delta \lesssim 0$.

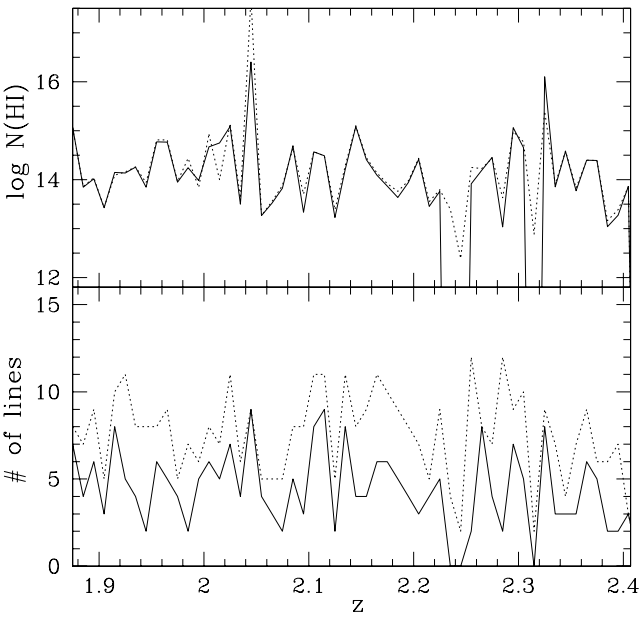

Figure 9. Comparison between the fitting results by FITLYMAN (solid line) and VPFIT (dotted line) for the QSO Q0109−3518. The lower panel shows the total number of lines, while the upper one shows the sum of the column densities of all the lines in redshift bins of width $\Delta z = 0.01$.The two redshift intervals where the column density measured with FITLYMAN goes to zero correspond to masked metal lines falling at those redshifts.

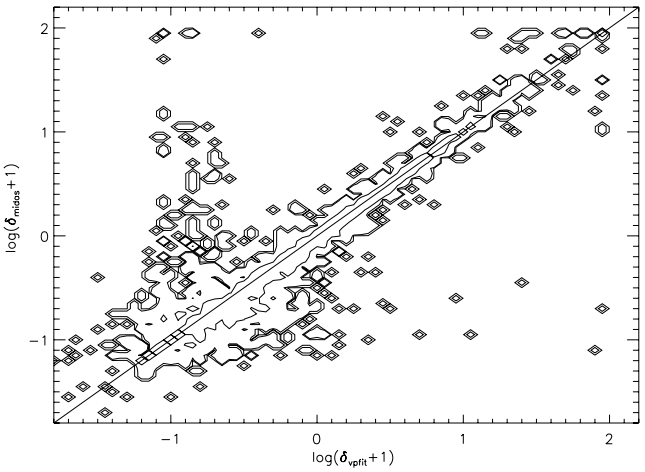

Figure 10. Contour scatter plot of the FITLYMAN versus VPFIT reconstructed density fields. The contours show the number density of pixels which increases by a factor of 10 at each level.

4 SIMULATED DATA SAMPLE

We use simulations run with the parallel hydrodynamical (TreeSPH) code GADGET-2 based on the conservative 'entropy formulation' of SPH (Springel 2005). They consist of a cosmological volume with periodic boundary conditions filled with an equal number of dark matter and gas particles. Radiative cooling and heating processes are followed for a primordial mix of hydrogen and helium. We assume a mean ultraviolet background produced by QSOs and galaxies as given by Haardt & Madau (1996) with helium heating rates multiplied by a factor of 3.3 in order to better fit observational constraints on the temperature evolution of the IGM. This background gives naturally a $\Gamma \sim 10^{-12}$ (H ionization rate) at the redshifts of interest here (Bolton et al. 2005). The star formation criterion is a very simple one that converts in collisionless stars all the gas particles whose temperature falls below 10^5 K and whose density contrast is larger than 1000 (it has been shown that the star formation criterion has

a negligible impact on flux statistics). More details can be found in Viel et al. (2004).

We use 2×400^3 dark matter and gas particles in a $120\,h^{-1}$ comoving Mpc box (although for some cross-checks we analyse some smaller boxes of $60\,h^{-1}$ comoving Mpc). The gravitational softening is set to $5\,h^{-1}$ kpc in comoving units for all particles.

We stress that the parameters chosen here, including the thermal history of the IGM, are in reasonably good agreement with observational constraints including recent results on the CMB and other results obtained by the Lyα forest community (e.g. Viel, Haehnelt & Lewis 2006).

The 120 Mpc simulation box at $z = 2$ is pierced to create a set of 364 mock lines of sight covering a redshift range $\Delta z \simeq 0.11$. For each of these lines of sight, we know the density contrast, the temperature and the peculiar velocity pixel by pixel. Peculiar velocities are small, typically less than 100 km s^{-1}, and randomly oriented, so their contribution, e.g. to the correlation function, is in general negligible. However, since we want to compare the result of simulations and observations, we modify the redshifts of the density field ($z_{\rm old}$) with the peculiar velocity field to obtain the density field in redshift space ($z_{\rm new}$) using the formula $v_{\rm pec}(z_{\rm old}) = c\,(z_{\rm new} - z_{\rm old})/[1 + (z_{\rm new} + z_{\rm old})/2]$. We added to the simulated spectra a Gaussian noise S/N = 50, in order to reproduce the observed average S/N per pixel. The simulated lines of sight have been fitted with Voigt profiles using an automated version of VPFIT.

4.1 Reconstruction of the δ field

The Lyα lines in each simulated line of sight are selected to have, as in the case of observations, $b \geqslant 10$ km s^{-1}. We introduce a further constraint, $b \leqslant 100$ km s^{-1}, which is required by the fact that simulated spectra are not continuum fitted. Shallow and broad oscillations in simulated spectra are fitted as absorption lines with Doppler parameters of the order of thousands of km s^{-1}. In the real spectra these kind of oscillations are instead fitted with the continuum and b parameters that large are not measured. The selected lines are grouped into absorbers and transformed into the corresponding density field following the procedure described in Section 3. In equation (1) the values $T_0 = 1.8 \times 10^4$ K and $\alpha = 0.6$ are adopted, which are consistent with an early re-ionization epoch and are the ones inferred from the simulations.

The reconstructed field is compared with the original density field (i.e. the output of the simulation), which is also binned into 1 $L_{\rm J}$ steps. An upper threshold is adopted both for the true and the recovered δ field, $\delta_{\rm thr} = 50$, since 99.95 per cent of pixels in the simulated lines of sight have values $\delta \leqslant \delta_{\rm thr}$ and the algorithm to recover the δ field (equation 1) is valid for values of $\delta \leqslant$ few $\times$ 10. The upper cut is applied before the normalization process.

The average values of the δ field considering all the 364 simulated spectra are $\langle\delta + 1\rangle \simeq 0.9$ and 1.3 for the true and recovered field, respectively. The fields are normalized using these values.

Fig. 11 shows the contour scatter plot of the original versus reconstructed density field. As can be seen from the figure, FLO reconstructs fairly well the original field above the mean density, while underdensities are underestimated, or not recovered, if they are below our lower threshold. Indeed, the lower horizontal tail observed in the scatter plot is due to the treatment of the empty bins during the absorber-field transformation. The upper horizontal tail is instead due to the cut applied to overdensities larger than the threshold, $\delta_{\rm thr}$. Fig. 12 shows the distribution of δ values in the true and recovered field. The peak at $\log(\delta + 1) \simeq -0.83$ contains $\simeq$53 per cent of all the points and it is due to the procedure that assigns to empty bins the value of δ corresponding to the redshift of the bin and to the minimum observed column density, $\log N({\rm H\,I}) = 12\,{\rm cm}^{-2}$. On the other hand, the small bump at $\log(\delta + 1) \simeq 1.57$ is due to the upper cut applied to the recovered density field and it includes $\sim$0.4 per cent of the total number of points.

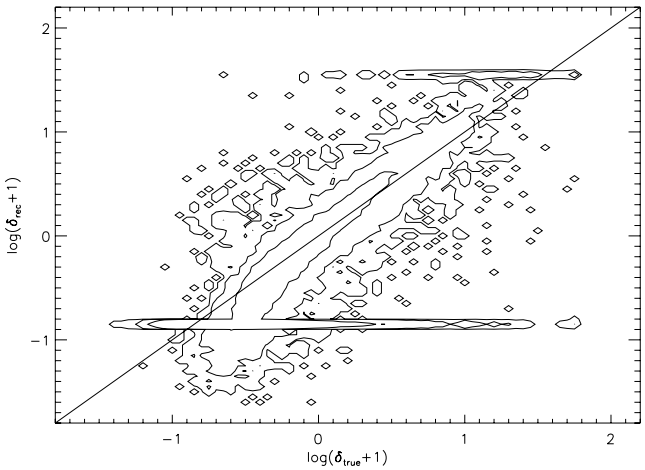

Figure 11. Contour scatter plot of the true versus reconstructed δ field from simulations. The contours show the number density of pixels which increases by a factor of 10 at each level.

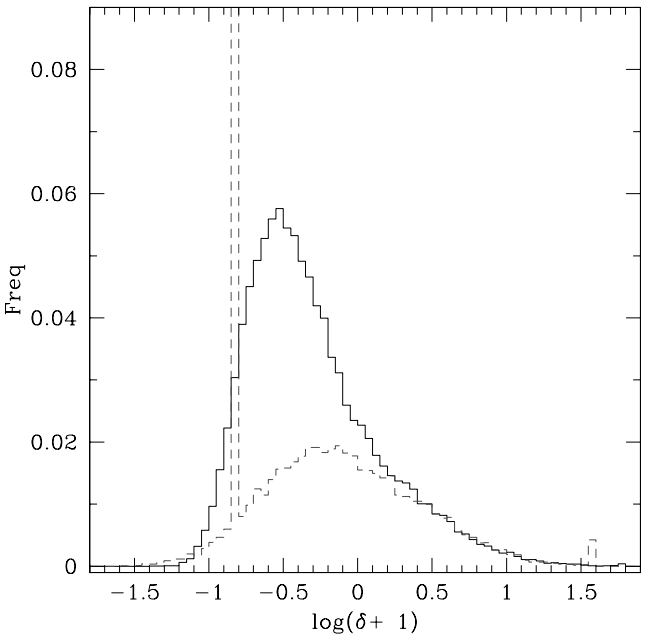

Figure 12. Distribution of δ values in the true (solid line) and recovered (dashed line) field normalized to the total number of points.

The transformation starts to recover more than half of the correct values of δ at $\log(\delta + 1) \simeq -0.15$ and recovers all the δ within 30 per cent in the range $-0.08 \lesssim \log(\delta + 1) \lesssim 1.45$. Clearly, we are not dealing correctly with the underdense regions, even if they are above our observational detection limit. This is likely due to the fact that our primary hypothesis, the local hydrostatic equilibrium, is not valid for those regions. This was also discussed by Schaye (2001) and here we have the evidence that under the mean density the gas is still expanding.

In the next section, it will be shown that the inaccuracies in the underdensity regime do not significantly affect statistical measures like the correlation function.

4.2 Two-point statistics of the δ field

We computed the correlation function for the original and recovered δ field, with the formula

$$\xi_\delta(r) = \langle \delta(r + \mathrm{d}r)\delta(r) \rangle, \tag{4}$$

where r is the physical separation of two points in comoving Mpc. $\xi_\delta(r)$ quantifies the clustering properties of the considered field, showing a signal significantly different from zero at separations where the field presents structures (overdensities or underdensities).

The bin size is the largest value of L_J for our sample, $\simeq$1.532 comoving Mpc, corresponding to the minimum redshift.

Fig. 13 plots the results of the correlation function for the true and recovered δ field. The value in each bin is the median value of 50 sample of 88 lines of sight obtained with a bootstrap technique from the 364 lines of sight of the total sample. This procedure is required in order to compare this result with the analogous one for the observed data (see Section 5.1). We have 22 observed spectra but each one covers a redshift range corresponding to about four simulated spectra. Error bars are 1σ, computed with the percentiles of the distribution of values in each bin. The recovered correlation function is in very good agreement with the true one at every separation.

We also estimate the 1D power spectrum of the hydrogen density contrast field, which is defined by the Fourier transform of the correlation function

$$\xi(r) = \frac{V}{2\pi} \int |\delta_k|^2 \mathrm{e}^{-\mathrm{i}kr} \mathrm{d}k \qquad P_\delta^{\mathrm{1D}}(k) \equiv \left\langle |\delta_k|^2 \right\rangle. \tag{5}$$

The power spectrum is computed adopting the fast Fourier transform (FFT) technique which requires that the field to be transformed is evenly sampled. To this purpose, we have rebinned the observed lines of sight to a constant step equal to the minimum Jeans length for the considered Lyα forest (corresponding to the maximum redshift). Then, the following steps have been applied.

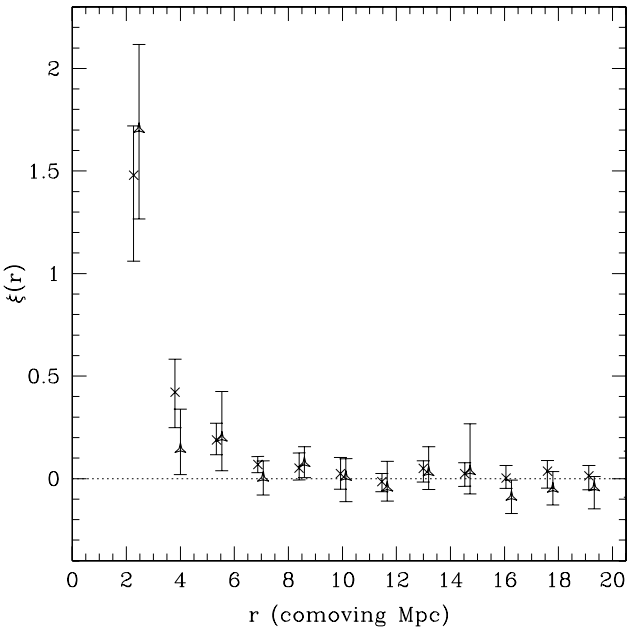

Figure 13. Correlation function of δ from simulations. Crosses represent the correlation function obtained from the original data, triangles the one obtained from the reconstructed field.

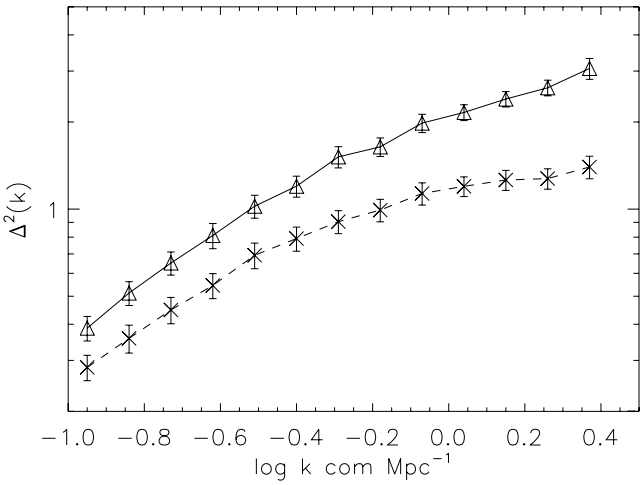

Figure 14. 1D power spectrum of the hydrogen density contrast field. The solid and the dashed lines represent the results for the reconstructed and the original δ field, respectively.

(1) A grid of wavenumbers is built in the Fourier space, starting from $k_{\min} = 2\pi/\Delta r$, where Δr is the length of a line of sight in comoving Mpc, and formed by $n_{\mathrm{pix}}/2$ evenly spaced elements, where n_{pix} is the number of pixels of the original δ field.

(2) The Fourier transform of the δ field is computed.

(3) The products $\delta_k \delta_{k'}$ are averaged in each bin.

(4) The $P_\delta^{\mathrm{1D}}(k)$ is normalized by multiplying it for the line of sight length, Δr.

(5) The obtained $P_\delta^{\mathrm{1D}}(k)$ is smoothed on larger bins to reduce the noise.

(6) The result is averaged over all the lines of sight.

Error bars are computed using a jackknife estimator (Bradley 1982) on the whole sample of simulated lines of sight.

Fig. 14 shows the results of the computation of the corresponding $\Delta^2(k) = kP_\delta^{\mathrm{1D}}(k)/2\pi$ for the true and recovered simulated δ fields. The two power spectra are consistent at the 3σ level on scales $20 \lesssim r \lesssim 60$ comoving Mpc.

5 FLO APPLIED TO THE OBSERVED DATA SAMPLE

In Section 2.1, we have described how the line lists are compiled for the 22 high-resolution QSO spectra forming our sample. The procedure explained in Section 3 is then applied to obtain the corresponding density contrast field for each line of sight. In the case of observations, we have to take into account the presence of the masked intervals covering regions occupied by metal absorption systems. We eliminate all the bins that are covered by more than 30 per cent by masked intervals. Before the normalization step, we apply an upper threshold as in the case of simulations ($\delta_{\mathrm{thr}} = 50$) since we want to compare our result with the one obtained in Section 4.2. The pixels above the threshold correspond to $\sim$0.9 per cent of the total number of pixels. Figs 10 and 11 show the uncertainties associated with the use of a different fitting tool (in particular, VPFIT and FITLYMAN) and the ones intrinsic to FLO, respectively. Since the intrinsic errors turn out to be larger than those induced by the

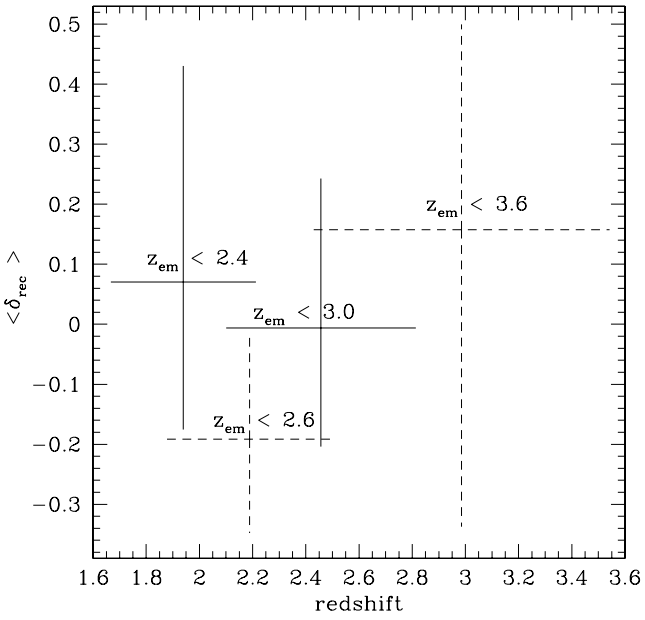

Figure 15. Distribution with redshift of the average reconstructed δ values for four subsamples of QSOs selected by their emission redshift as displayed in the plot (formed by six, six, five and five objects as redshift increases). Horizontal lines represent the redshift coverage of each QSO sample, while vertical lines are the spread in average δ values for the single QSOs in the samples.

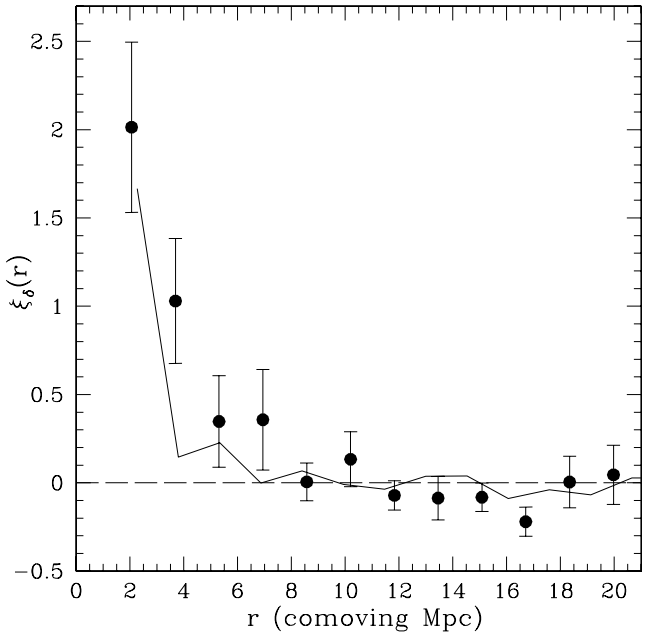

Figure 16. Correlation function of the δ field reconstructed from our 22 observed QSO spectra. Points refer to the data, the line instead represent the prediction from the simulation.

fitting technique, we can safely compare the results obtained from the simulations and those obtained from the data sample, presented in this section.

Fig. 15 shows the average values of the recovered δ fields for four subsamples built from the 22 observed lines of sight selected on the ground of the QSO emission redshifts. The spread of average δ values for the single QSOs forming the samples is also shown. There is no significant trend with redshift, as it is expected if the density field follows on average the evolution of the cosmic mean value.

5.1 Two-point statistics of the δ field

The correlation function for the observed δ field is computed with the formula given in equation (4) as for simulations.

The result is shown in Fig. 16. Here the value in each bin is obtained averaging all the sample, while the error bars are computed creating 50 samples of 22 lines of sight drawn out of our sample with a bootstrap technique and taking the percentiles of the distribution corresponding to 1σ errors. The bin size is $\simeq$1.6 comoving Mpc which is the L_J at the lowest redshift of the sample. The clustering signal is significant at more than the 3σ level in the first two bins ($r \lesssim 4.5$ comoving Mpc). We have superimposed to the data points the TPCF obtained from the recovered δ field of simulations. The two correlation functions are in very good agreement, confirming the validity of the cosmological parameters adopted in the simulation.

Since $P_\delta^{1D}(k)$ is very sensitive to cosmological parameters, it is very important to check if the prediction of such a function are in agreement with the observed values.

In the case of the observed spectra, the masked metal lines make the starting grid of pixels unevenly spaced, thus not fitted for the application of the FFT. To overcome this problem, as a first-order approximation, the masked bins have been put to the average density. This procedure is based on the observation that the Lyα forest gas traces on average the average density and on the analogous method adopted in the computation of the power spectrum of the transmitted flux (Viel et al. 2004). Fig. 17 shows the result of this computation: the power spectrum obtained from our data is in excellent agreement with the one obtained from the density fields reconstructed with FLO from the simulated spectra based on a concordance cosmological model. Error bars are computed using a jackknife estimator on the whole sample of observed QSOs. The quantity which is generally compared with the model predictions is the 3D power spectrum, which is obtained from the 1D by differentiation, $P_\delta^{3D}(k) = -(2\pi/k)\mathrm{d}P_\delta^{1D}(k)/\mathrm{d}k$. A comparison of the rough estimates of $P_\delta^{3D}(k)$ from our observed and simulated data gives good agreement. However, we postpone a careful study of this quantity

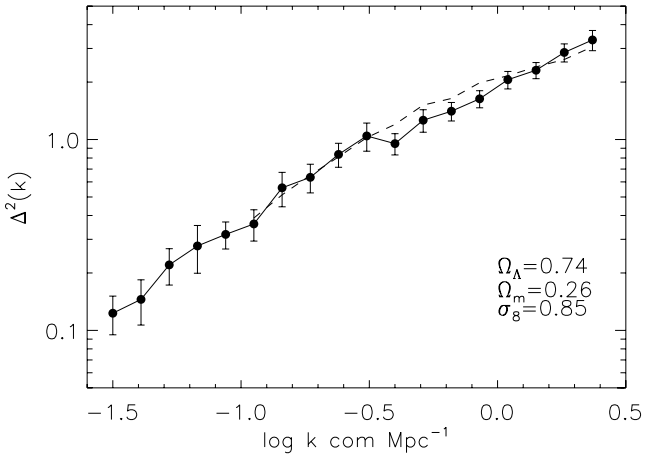

Figure 17. Power spectrum of the δ field reconstructed from our 22 observed QSO spectra. The dashed line represents the prediction from the simulation.

obtaining constraints on the cosmlogical parameters to a forthcoming paper.

6 CONCLUSIONS

We have presented results from the analysis of the largest sample of fitted Lyα lines obtained from 22 high-resolution QSO spectra covering the redshift range between $\sim$1.7 and 3.5.

In particular, we have computed the following.

(1.i) The line number density evolution with redshift for which we find $\mathrm{d}n/\mathrm{d}z \simeq (166 \pm 4)[(1+z)/3.5]^{2.8\pm0.2}$. While the redshift evolution is consistent with previous results, the normalization is higher by a factor ranging from $\sim$0.03 in $\log(\mathrm{d}n/\mathrm{d}z)$ at $z \sim 2$ to 0.1 at $z \sim 3$. This difference is due to the improved treatment of the contamination by metal lines (amounting to $\sim$9 per cent of the redshift interval covered by the Lyα forests), which is made possible by the high resolution and S/N of our spectra. Consistently with Kim et al. (2002), we also find a steeper evolution for the stronger lines [$14.5 \leqslant \log N(\mathrm{H\,I}) < 17$] compared to the weak ones [$13 \leqslant \log N(\mathrm{H\,I}) < 14$].

(1.ii) The TPCF which shows a significant clustering signal up to $\sim$2 comoving Mpc for strong lines [$13.8 \leqslant \log N(\mathrm{H\,I}) < 17$], and also for weak lines [$12 \leqslant \log N(\mathrm{H\,I}) < 13.8$] although on smaller scales, $\lesssim$1.5 Mpc. We then calculated the TPCF by grouping all the lines closer than the local Jeans length (the assumed typical size for the hydrogen absorbers in the IGM). The signal is still significant in the first bin ($r \lesssim 2.5$ Mpc).

(1.iii) The TPCF evolution with redshift for strong lines: we divided our sample in two subsamples; the first one, formed by objects with $z_{\mathrm{em}} \lesssim 2.5$, for which the average Lyα forest redshift is $\langle z_{\mathrm{Ly}\alpha}\rangle = 2.07$, and the second one, formed by objects with $z_{\mathrm{em}} > 2.5$, with $\langle z_{\mathrm{Ly}\alpha}\rangle = 3.02$. The TPCF computed for lines with $13.8 < \log N(\mathrm{H\,I}) < 17$ in these two samples, show a trend of increasing clustering with decreasing redshift; this is an apparent evolution, due to the fact that the relation $\delta - \log(N(\mathrm{H\,I}))$ is z dependent. Indeed a selection of lines tracing the same kind of structures (characterized by $\delta > 3$) shows no evidence of a significant evolution with redshift of the TPCF.

In the second part of the paper, we have described FLO, a new algorithm to transform the measured H I column densities of the Lyα lines detected along a line of sight, into the underlying total H density field (and in particular, the density contrast, $\delta \equiv n_{\mathrm{H}}/\langle n_{\mathrm{H}}\rangle - 1$, field). The method is based on the assumption that Lyα absorbers are in local hydrostatic equilibrium and, as a consequence, the Jeans length corresponds to their characteristic size. The aim of this study is to find a robust statistical estimator which allows a direct link to the physical properties of the gas and an easy comparison with the results of simulations. To test the effects of the transformation, we have used a set of 364 lines of sight obtained from a large N-body hydrodynamical simulation run in a box of $120\,h^{-1}$ comoving Mpc. For every line of sight we have both the density and velocity field pixel per pixel and the list of Voigt fitted Lyα lines with central redshift, column density and Doppler parameter. Our results can be summarized as follows.

(2.i) FLO recovers extremely well (within 30 per cent) the overdensities up to $\delta \sim 30$ while it is not reproducing correctly the underdensities (more than 50 per cent of δ values are not recovered) even in the range above our resolution limit. This result suggests that the hypothesis of hydrostatic equilibrium is not valid for the underdense regions that are likely still expanding. On the other hand, for the goal of our study, that is the computation of statistical properties of the IGM, the resulting δ field gives satisfactory results when the TPCF and the 1D power spectrum are considered. The comparison of the results obtained with the true δ field of the simulation and with the one reconstructed from line column densities with our algorithm, are in very good agreement.

When applied to the observed data sample, the FLO technique gives the following results.

(2.ii) The redshift distribution of the average hydrogen density is consistent with the evolution of the cosmic mean hydrogen density in the redshift range covered by our QSO sample, supporting the fact that the Lyα forest arises from fluctuations of the IGM close to the mean density.

(2.iii) The correlation function of the density field obtained from the observed spectra shows a significant clustering signal up to $\sim$4 comoving Mpc and is consistent with the analogous result obtained for the recovered density field in a simulation based on the concordance cosmological model.

(2.iv) The 1D power spectrum of the δ field obtained from the observed spectra is in very good agreement with the same result obtained from the recovered density field from the simulation based on the concordance cosmological model on scalelengths between $\sim$2.5 and 63 comoving Mpc.

The algorithm presented in this work is particularly useful to extract information from observations in terms of overdensities, making it possible a more direct and handy comparison with simulations.

ACKNOWLEDGMENTS

Hydrodynamical simulations were done at the UK National Cosmology Supercomputer Centre funded by PPARC, HEFCE and Silicon Graphics/Cray Research and at the HPCF (Cambridge High Performance Computer Cluster). We are grateful to Tae-Sun Kim for permission of using her lists of fitted QSO absorption lines before publication. HIRES data were obtained at the W. M. Keck Observatory, which was made possible by the generous financial support of the W. M. Keck Foundation, and operated as a scientific partnership among the California and the National Aeronautics and Space Administration.

REFERENCES

Aracil B., Petitjean P., Pichon C., Bergeron J., 2004, A&A, 419, 811
Bechtold J., Crotts A. P. S., Duncan R. C., Fang Y., 1994, ApJ, 437, L83
Becker G. D., Sargent W. L. W., Rauch M., 2004, ApJ, 613, 61
Bergeron J. et al., 2004, The Messenger, 118, 40
Bi H.-G., Davidsen A. F., 1997, ApJ, 479, 523
Bolton J. S., Haehnelt M. G., Viel M., Springel V., 2005, MNRAS, 357, 1178
Bond J. R., Kofman L., Pogosyan D., 1996, Nat, 380, 603
Bradley E., 1982, The Jackknife, the Bootstrap and Other Resampling Plans, SIAM, Philadelphia
Cen R., Miralda-Escudè J., Ostriker J. P., Rauch M., 1994, ApJ, 437, L83
Chand H., Srianand R., Petitjean P., Aracil B., 2004, A&A, 417, 853
Coppolani F. et al., 2006, MNRAS, 370, 1804
Cristiani S., D'Odorico V., 2000, AJ, 120, 1648
Cristiani S., D'Odorico S., Fontana A., Giallongo E., Savaglio S., 1995, MNRAS, 783, 1016
Cristiani S., D'Odorico S., D'Odorico V., Fontana A., Giallongo E., Savaglio S., 1997, MNRAS, 285, 209

Croft R. A. C., Weinberg D. H., Pettini M., Hernquist L., Katz N., 1999, ApJ, 520, 1
Crotts A. P. S., Fang Y., 1998, ApJ, 502, 16
Davé R., Hernquist L., Weinberg D. H., Katz N., 1997, ApJ, 477, 21
Dekker H., D'Odorico S., Kaufer A., Delabre B., Kotzlowski H., 2000, in Masanori I., Moorwood A. F., eds, Proc. SPIE Vol. 4008, Optical and IR Telescope Instrumentation and Detectors. SPIE, Bellingham, p. 534
Dinshaw N., Weymann R. J., Impey C. D., Foltz C. B., Morris S. L., Ake T., 1997, ApJ, 491, 45
D'Odorico V., Cristiani S., D'Odorico S., Fontana A., Giallongo E., Shaver P., 1998, A&A, 339, 678
D'Odorico V. et al., 2006, MNRAS, 372, 1333
Fang Y., Duncan C., Crotts A. P. S., Bechtold J., 1996, ApJ, 462, 77
Fontana A., Ballester P., 1995, The Messenger, 80, 37
Giallongo E., Cristiani S., D'Odorico S., Fontana A., Savaglio S., 1996, ApJ, 466, 46
Haardt F., Madau P., 1996, ApJ, 461, 20
Hernquist L., Katz N., Weinberg D. H., Miralda-Escudé J., 1996, ApJ, 457, L51
Hui L., Gnedin N. Y., 1997, MNRAS, 292, 27
Kim T.-S., Cristiani S., D'Odorico S., 2001, A&A, 373, 757
Kim T.-S., Carswell R. F., Cristiani S., D'Odorico S., Giallongo E., 2002, MNRAS, 335, 555
Kirkman D., Tytler D., 1997, ApJ, 484, 672
Lu L., Sargent W. L. W., Womble D. S., Takada-Hidai M., 1996, ApJ, 472, 509
Machacek M. E., Bryan G. L., Meiksin A., Anninos P., Thayer D., Norman M., Zhang Y., 2000, ApJ, 532, 118
McDonald P., Miralda-Escudé J., Rauch M., Sargent W. L. W., Barlow T. A., Cen R., Ostriker J. P., 2000, ApJ, 543, 1
McLean B. J., Greene G. R., Lattanzi M. G., Pirenne B., 2000, in Manset N., Veillet C., Crabtree D., eds, ASP Conf. Ser. Vol. 216, Astronomical Data Analysis Software and Systems IX. Astron. Soc. Pac., San Francisco, p. 145
Miralda-Escudé J., Cen R., Ostriker J. P., Rauch M., 1996, ApJ, 471, 582
Misawa T. et al., 2004, AJ, 128, 2954
Nusser A., Haehnelt M., 1999, MNRAS, 303, 179
Peebles P. J. E., 1980, The Large Scale Structure of the Universe. Princeton Univ. Press, Princeton, NJ
Petitjean P., Surdej J., Smette A., Shaver P., Mücket J., Remy M., 1998, A&A, 334, L45
Rauch M., Sargent W. L. W., Womble D. S., Barlow T. A., 1996, ApJ, 467, L5
Rauch M., Sargent W. L. W., Barlow T. A., Carswell R. F., 2001, ApJ, 562, 76
Rauch M., Becker G. D., Viel M., Sargent W. L. W., Smette A., Simcoe R. A., Barlow T. A., Haehnelt M. G., 2005, ApJ, 632, 58
Rollinde E., Petitjean P., Pichon C., Colombi S., Aracil B., D'Odorico V., Haehnelt M. G., 2003, MNRAS, 341, 1279
Sargent W. L. W., Young P. J., Boksenberg A., Tytler D., 1980, ApJS, 42, 41
Schaye J., 2001, ApJ, 559, 507
Smette A., Surdej J., Shaver P. A., Foltz C. B., Chaffee F. H., Weymann R. J., Williams R. E., Magain P., 1992, ApJ, 389, 39
Smette A., Robertson J. G., Shaver P. A., Reimers D., Wisotzki L., Koehler T., 1995, A&AS, 113, 199
Spergel N. et al., 2007, ApJS, 170, 377
Springel V., 2005, MNRAS, 364, 110
Theuns T., Leonard A., Efstathiou G., 1998, MNRAS, 297, L49
Tytler D., 1987, ApJ, 321, 69
Tytler D., Fan X.-M., 1992, ApJS, 79, 1
Viel M., Matarrese S., Mo H. J., Haehnelt M., Theuns T., 2002, MNRAS, 329, 848
Viel M., Haehnelt M. G., Springel V., 2004, MNRAS, 354, 684
Viel M., Haehnelt M. G., Lewis A., 2006, MNRAS, 370, L51
Weymann R. J. et al., 1998, ApJ, 506, 1
Young P. A., Impey C. D., Foltz C. B., 2001, ApJ, 549, 76
Zaroubi S., Viel M., Nusser A., Haehnelt M., Kim T.-S., 2006, MNRAS, 369, 734
Zhang Y., Anninos P., Norman M. L., 1995, ApJ, 453, L57
Zhang Y., Anninos P., Norman M. L., Meiksin A., 1997, ApJ, 485, 496

This paper has been typeset from a TEX/LATEX file prepared by the author.